Amorphization along interfaces and grain boundaries in polycrystalline multilayers: An x-ray-diffraction study of Ni/Ti multilayers

Mark A. Hollanders, Barend J. Thijsse, and Eric J. Mittemeijer
Laboratory of Metallurgy, Delft University of Technology, Rotterdamseweg 137, 2628 AL Delft, The Netherlands
(Received 25 September 1989; revised manuscript received 13 April 1990)

Diffusion-induced solid-state amorphization (SSA) was studied in (fcc Ni)/(hcp Ti) multilayers at 523 K. The multilayers had a modulation length of 24.4 nm and an overall composition of $Ni_{40}Ti_{60}$. They were polycrystalline without coherency between the Ni and Ti sublayers. The phase changes, composition changes, and strain development were studied for annealing times up to 220 h, primarily using x-ray-diffraction methods. Upon annealing, an amorphous phase developed, concurrently with dissolution of Ti in crystalline Ni. The amorphous phase not only formed along the Ni/Ti interfaces, but also along the grain boundaries in the sublayers. Continued amorphization along the original grain boundaries on prolonged annealing implies that fast-diffusion paths in the amorphous phase remained active. Diffusion coefficients were determined, using methods described in a separate paper. The interdiffusion coefficient for the amorphous phase is smaller than the tracer-diffusion coefficient of Ni in hcp Ti and larger than the chemical diffusion coefficient in fcc (Ni,Ti) solid solutions. The reaction virtually stopped after 16 h, when appreciable amounts of crystalline Ni and Ti were still present, which is ascribed to ordering in the crystalline (Ni,Ti) solid solution. Both the dissolution of Ti in crystalline Ni and the amorphization are associated with the development of stress profiles in the multilayer. These are quantitatively discussed and analyzed using the x-ray-diffraction and Fizeau interferometric data.

I. INTRODUCTION

The discovery, in 1983,[1] of amorphous-phase formation by interdiffusion in an assembly of different crystalline metallic components evoked great interest (for a review, see Ref. 2). Systems exhibiting solid-state amorphization (SSA) are thought to obey two criteria: (1) a large negative Gibbs free energy of mixing, and (2) "anomalously" fast diffusion of one of the constituents.

In this work results are presented on the kinetics of SSA. For two reasons the Ni-Ti system was selected.

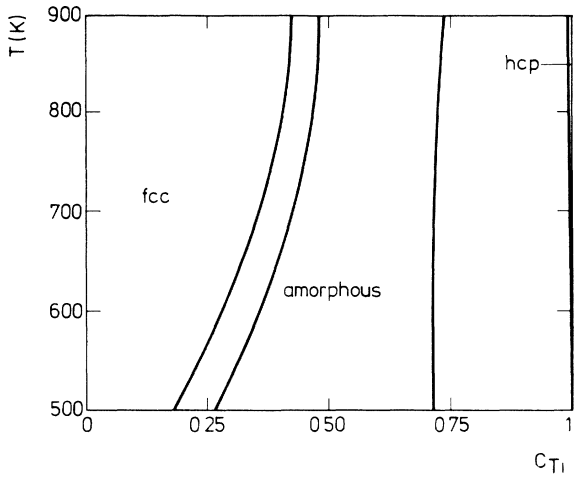

FIG. 1. Metastable phase diagram of the Ni-Ti system, taking into account only the amorphous phase and the terminal solid solutions (Ref. 3). c_{Ti} denotes the atomic fraction of Ti.

First, a recent calculation of a metastable phase diagram,[3] only considering crystalline terminal solid solutions and an amorphous phase, shows (i) a fairly wide concentration range where the amorphous phase is more stable than the crystalline terminal solid solutions, and (ii) a considerable metastable solid solubility of Ti in crystalline Ni (Fig. 1). Secondly, anomalously fast diffusion of Ni in α-Ti in the temperature range 912–1141 K has been reported.[4] Previous work has already indicated that amorphization can occur in this system.[5,6]

In the present paper the behavior of Ni/Ti multilayers upon isothermal annealing is analyzed. The multitude of interfaces and thus the large reaction area make multilayers convenient systems to study SSA. X-ray diffractometry is employed as the main experimental method. It will be demonstrated that dissolution of Ti in Ni occurs simultaneously with the formation of the amorphous phase, and that this takes place both along the original interfaces and along the grain boundaries in the individual layers. The phase transformations are associated with stress development and relaxation.

II. EXPERIMENT

A. Multilayer preparation and annealing treatments

Samples were prepared by magnetron sputtering in a Leybold-Hereaus LH 550 apparatus with a base pressure below 5×10^{-4} Pa and a 2 Pa Ar plasma. The deposition rates were calibrated using an Alfa Step 2000 thickness meter and amounted to 12 nm/min for Ni (190 W dc) and 8 nm/min for Ti (475 W rf). To get sharp interfaces, the sputtering process was interrupted after the deposition of

TABLE I. Annealing treatments (at 523 K) of the Ni/Ti multilayers.

Specimen	Time step	Time domain
1	15 min	0–210 min
	30 min	210 min to 6 h
	5 h	6–16 h
2	16 h	0–64 h
	78 h	64–220 h

each Ni sublayer and of each Ti sublayer. The multilayers consisted of 20 periods of approximately 8 nm Ni and 16 nm Ti. Single-crystal Si{100} wafers with a diameter of 2 in. and a thickness of 280 μm with a {110}-orientation flat (reference side) were used as substrates; they were covered with a sputter-deposited 200-nm-thick-layer, amorphous-SiO_2 diffusion barrier. During sputtering the substrate was positioned in such a way that the line joining the centers of the sputter table and wafer was also a normal of the orientation flat between both centers. The maximum temperature of the specimens during sputtering was estimated at about 373 K.

Electron-probe microanalysis (EPMA) indicated an overall composition of the multilayer of $Ni_{40}Ti_{60}$, consistent with the values for the Ni and Ti sublayer thicknesses. No contaminations of C or Ar were detected. Auger depth profiling indicated that O contamination had occurred only in the top Ti sublayer (about 5–10 at. %), indicating that the O was introduced after sputtering. This appears to be unavoidable in practice.[4,7]

Slabs of 26 mm width were cut from the center of the specimens, parallel to the orientation flat, using a diamond-pointed pen. Two samples were annealed at 523±2 K in steps up to total annealing times of 16 and 220 h, in a furnace containing a purified Ar atmosphere. The annealing treatments are listed in Table I. After some annealing treatments, the curvature of the specimen was measured with a laboratory-built Fizeau interferometer using Hg light.

B. X-ray diffractometry and transmission electron microscopy

X-ray diffraction analysis was performed in reflection geometry on Siemens F and D-500 ω diffractometers, using Cr $K\alpha$ and Cu $K\alpha$ wavelengths. Soller slits and a graphite monochromator were located in the diffracted-beam path. Measurements were performed with and without ω tilt. Experimental details are given in Table II. A special specimen holder was developed for the low-angle measurements ($2\theta < 10°$), in order to place the specimens as reproducibly and as flat as possible in the diffractometer. The low-angle range was measured in overlapping scans with different divergence slits to ensure irradiation of the complete length of the specimen at all times. The x-ray tube current was varied between 6 and 30 mA at a voltage of 40 kV to prevent counting rates too high for the detector (i.e., $> 10^4$ Hz). The high-angle measurements were performed at 40 kV and 30 mA. A Si polycrystal standard was measured regularly to correct for systematic changes in incident-beam intensity and instrument alignment.

The preparation of planar view and cross-sectional transmission-electron-microscopy (TEM) specimens will be described elsewhere.[8] TEM analysis was performed with a Philips EM 400T microscope operating at 120 kV.

III. RESULTS AND INTERPRETATION

The high-angle diffraction pattern of an as-prepared specimen is shown in Fig. 2. The two main peaks are α-Ti{002} and Ni{111}. Five parameters were determined for both peaks as a function of annealing time: the position of the maximum, $2\theta_{max}$, the maximum intensity I_{max}, the integrated intensity I_{int}, and the left ($2\theta < 2\theta_{max}$) and right ($2\theta > 2\theta_{max}$) widths at half of I_{max}, w_l and w_r. To minimize the effects of peak overlap, the integrated intensity, I_{int}, was estimated for Ti{002} by taking twice the value of the left part of the peak and for Ni{111} by taking twice the value of right part of the peak. The background intensity was determined by linear interpolation of the range extremities in the as-prepared condition (Fig. 2) and subtracted accordingly.

The peak parameters were used as follows. Values for the lattice spacing, d, were calculated from $2\theta_{max}$ according to Bragg's law. The produced or consumed amount of diffracting phase is proportional to I_{int}. This assumes that the texture and the scattering power per atom remain constant. The integral breadth $\beta \equiv I_{int}/I_{max}$ is inversely proportional to the size, Z, of the coherently diffracting domains, in a direction perpendicular to the diffracting planes, according to Scherrer's law: $Z = \lambda/\beta\cos\theta$.[9] The maximum possible value of Z is the

TABLE II. Characteristic radiations, 2θ ranges, step sizes, tilt angles, and slit widths used in the x-ray-diffraction experiments.

	Radiation $K\alpha$	2θ range (deg)	$\Delta 2\theta$ (deg)	ω (deg)	Divergence slit (deg)	Receiving slit (deg)
1	Cr	1–10	0.006	0	0.3–1.5	0.018
2	Cr	50–80	0.05	0	1.0	0.15
3	Cr	50–80	0.1	13	1.0	0.15
4	Cu	78–104	0.1	0	3.0	0.15
5	Cu	78–104	0.1	7	3.0	0.15

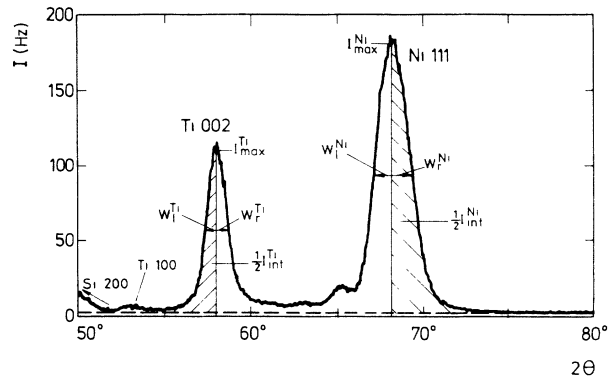

FIG. 2. X-ray-diffraction pattern of an as-prepared specimen (Cr $K\alpha$ radiation). Bragg peaks and peak parameters used in the analysis are indicated.

sublayer thickness, which is about 10 nm. The associated peak broadening is so large that other causes of peak broadening are likely of minor importance (see Sec. III C). If the peak shape remains constant during annealing, also a change of $2w = w_l + w_r$ is inversely proportional to a change of Z (this can be of use if systematic errors in the determination of β are expected). If a product phase would grow exclusively as a planar layer along the Ni/Ti interfaces, the relative changes of $1/2w$ and I_{int} should be identical. However, if a product phase would also grow along the grain boundaries in the sublayers, the relative change in I_{int} will be larger than that of $1/2w$. For reasons discussed below, the quantities $2w$ and I_{int} for Ni are calculated as $2w_r$ and $2w_r I_{\max}$, respectively, when interpreted in the way described above.

The low-angle diffraction pattern of an as-prepared sample is shown in Fig. 3. Here the Bragg peaks caused by the periodic composition modulation of length Λ occur; Λ is the sum of the Ni and Ti sublayer thicknesses. As discussed in a previous paper,[7] the composition profile can not be obtained directly from this pattern. However, values for Λ can be derived from the peak positions using a modified version of Bragg's law that takes into account the real part of the deviation of the refractive index from 1,[10] δ [$(m\lambda)^2 = 4\Lambda^2(\sin^2\theta_m - 2\delta)$, with m the order of reflection].

A. As-prepared specimens

The compositions modulation length Λ as obtained from the low-angle diffraction pattern was found to be 24.38 ± 0.10 nm. In combination with the overall composition data according to EPMA, Ni and Ti sublayer thicknesses of 7.2 and 17.2 nm are calculated.

Apart from the corresponding higher-order reflections and a weak α-Ti{100} reflection, no other peaks than Ni{111} and α-Ti{002} were observed: the layers have a sharp fiber texture with close-packed planes parallel to the Ni/Ti interfaces. The sharpness of the texture is also exhibited by the diffraction pattern recorded at tilt angle $\omega = 13°$ (cf. Figs. 2 and 4), indicating a drastic decrease in intensity of both peaks on tilting the specimen, and by the absence of the Ti{002} reflections in the electron-diffraction pattern of a *planar* section of a multilayer [Fig. 17(a)].

The lattice spacings calculated from the peak positions are $d_{\text{Ni}\{111\}} = 2.040$ Å and $d_{\text{Ti}\{002\}} = 2.362$ Å. These can be compared with the values 2.034 and 2.342 Å, respectively, obtained from the literature.[11] In particular, the measured value for Ti{002} is relatively large. This is ascribed to a compressive stress in the Ti sublayers parallel to the Ni/Ti interfaces; such a stress has been observed earlier for sputtered Ti.[12] The compressive nature of the overall stress was also manifested by the curvature of the specimen as revealed by Fizeau interferometry.

The small peaks at the low-angle side of the Ni{111} peak are interpreted as Laue satellites, implying a practically constant Ni-crystallite size in the direction perpendicular to the Ni/Ti interfaces (column length). The Laue interference function gives rise to satellites at both sides of the main peak.[9] However, calculation of line profiles (Fig. 5; also see subsection B) shows that if the spacing of the diffracting planes is larger at the top and bottom sides of a crystallite than in the middle, the satel-

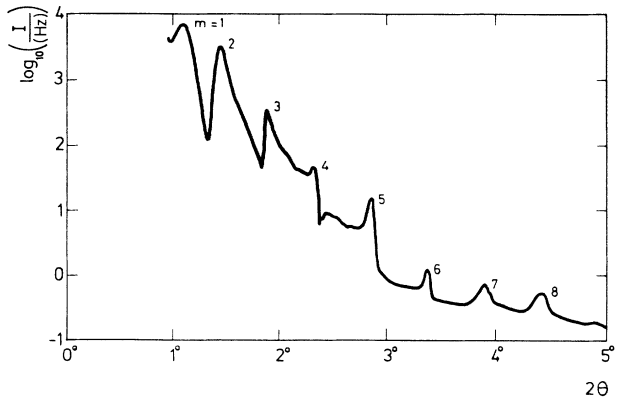

FIG. 3. Low-angle x-ray-diffraction pattern of an as-prepared specimen (Cr $K\alpha$ radiation). Note that the intensity scale is logarithmic. The orders m of the reflections, due to the composition modulation, are shown.

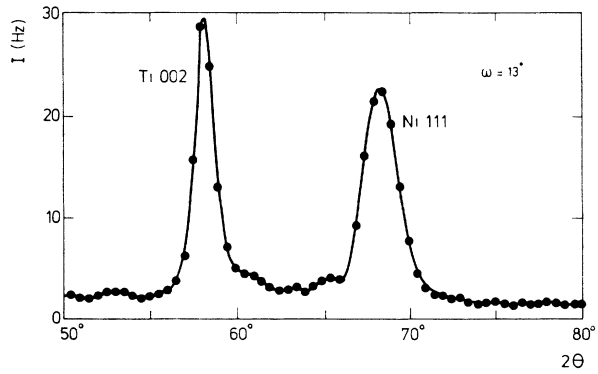

FIG. 4. X-ray-diffraction pattern of an as-prepared specimen with an ω tilt of 13° (Cr $K\alpha$ radiation). The corresponding pattern without tilt is shown in Fig. 2.

lites at the high-angle side of the main peak are decreased in intensity, whereas the satellites at the low-angle side are increased in intensity [cf. Figs. 5(a) and 5(b)]. Such spacing changes can be due to dissolution of Ti in the Ni crystallites near the Ni/Ti interfaces, since the Ni lattice parameter increases 0.1% per atomic percent of dissolved Ti.[13] This implies that in the as-prepared conditions some diffusion had already occurred.

The initial value of $2w/\beta$ is 0.89 for both Ni{111} and Ti{002}, which agrees with the value of $2w/\beta$ for the Laue interference function [0.886 (Ref. 14)] within experimental accuracy. This result is consistent with the above interpretation, in that the sublayers mainly consist of crystallites of size equal to the sublayer thicknesses in the direction of the layer normal.

The crystallite size Z for the Ni sublayers can be calculated from the positions of the maxima and minima of the satellites (the change of these positions owing to the nonuniformity of the spacings discussed above is negligible). It follows that $Z=7.31\pm0.06$ nm, in good agreement with the value of 7.2 nm derived from the overall composition (EPMA) and the multilayer period Λ. The, minor, positive difference is consistent with some Ti dissolved in the Ni layer, the absence of Laue satellites for the Ti{002} peak indicates that the Ti sublayers have a less uniform domain size than the Ni sublayers, implying the presence of Ti crystallites smaller than the sublayer thickness. (For Z obtained from Scherrer's equation, see Ref. 17.)

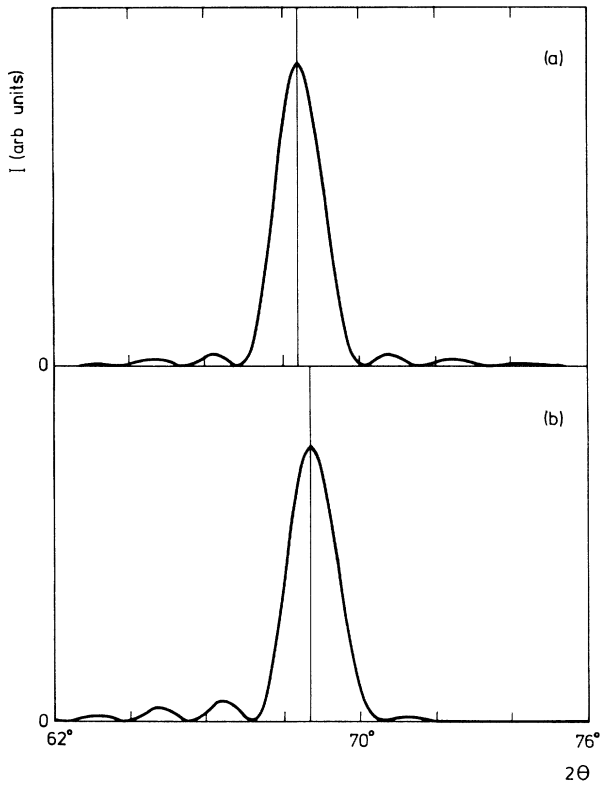

FIG. 5. Calculated diffraction patterns of crystallite composed of 50 Ni(111) planes parallel to the surface of the specimen, Bragg-Brentano geometry: (a) no Ti dissolved; (b) 20 at. % Ti dissolved in five top and five bottom planes, showing the effect of Ti dissolution in association with coherency strains on Laue satellites and on line position.

The TEM images (Fig. 6) reveal that the lateral dimensions of the crystallites are of the same order of magnitude as the sublayer thicknesses, i.e., 10 nm. In the TEM specimens for cross-sectional analysis the Ti was found to be hydrided, probably due to preparation artifacts, and no conclusions could be drawn concerning the perfection of the periodicity of the multilayer (linewidth analysis of the x-ray low-angle diffraction peaks indicates a Λ variation in the specimen of only 2.5%). The cross-sectional dark-field image [Fig. 6(d)] confirms that the individual layers mainly consist of crystallites whose sizes perpendicular to the interfaces are equal to the sublayer thicknesses.

From the combined x-ray-diffractometry (XRD) and TEM analyses it is concluded that the as-prepared multilayers consist of polycrystalline Ni and Ti sublayers constituted of approximately equiaxial crystallites of dimensions equal to the sublayer thickness. The high-angle diffraction pattern only shows peaks originating from diffraction by individual crystallites. No multilayer fringes characteristic for epitaxial multilayers occur. This means that the crystallites can be considered as diffracting incoherently. The Ti sublayers are subjected to a compressive stress. Some Ti is dissolved in the Ni sublayers near the interfaces. Between the two specimens no significant differences could be detected in the as-prepared condition.

B. Dissolution of Ti in Ni

The Ni{111} and α-Ti{002} peak positions are shown as a function of annealing time in Fig. 7. The largest changes occur for the Ni{111} peak position: in the first 30 min a pronounced increase, then a gradual decrease. The changes in Ti{002} peak position are much smaller: in the first 15 min a small increase, then a very gradual decrease, and eventually an increase again.

The behavior of the Ni{111} peak position can be explained by dissolution of Ti in Ni. The equilibrium Ni lattice spacing increases upon dissolution of Ti (see subsection A). Thus a decrease in peak position can be expected if Ti dissolves. However, in the first stages of dissolution the dissolved Ti is not homogeneously distributed in the Ni crystallites, as indicated by the occurrence of the Laue satellites at only the low-angle side of the main peak (see Sec. III A). As a consequence, the theoretical strain-free lattice spacing is not constant in a crystallite: it will be larger near the interfaces where the Ti is dissolved than it will be in the middle. Hence, coherency strains develop in the Ni crystallites: parallel to the interfaces, compressive stresses occur in the interface-adjacent regions, and tensile stresses occur in the center. Then, as compared to the strain-free lattice spacing, the lattice spacing parallel to the diffusion direction (i.e., perpendicular to the interfaces) will be larger in the interface-adjacent regions and smaller in the center [Fig. 8(b)]. This strain model implies that the lattice spacing

parallel to the interfaces in the Ni sublayer is constant. Its value can be calculated from a balance of forces over a section of the sublayer perpendicular to the interfaces. If it is assumed that the elastic constants do not depend on Ti content, this balance of forces reduces to a balance of strains.

On the above basis, the diffraction by the Ni sublayer upon dissolution of Ti can be calculated. For a certain composition profile, the constant lattice spacing and the associated strain profile, both parallel to the interfaces, are calculated. Adopting values for the elastic constants for monocrystalline Ni (Ref. 15) with {111} parallel to the interfaces, the corresponding stress profile and, finally, the depth distribution of the lattice spacing taken in the direction *perpendicular* to the interfaces are obtained. A result is shown in Fig. 5(b), for a Ni sublayer composed of 50 (111) planes parallel to the interfaces with 20 at. % Ti in the five top and five bottom planes. It can be seen that the position of the major peak maximum occurs at a larger diffraction angle than for pure Ni [cf. Figs. 5(a) and 5(b)]. The calculated effect is approximately equal to that measured after 30 min of annealing [see Fig. 7(b)].

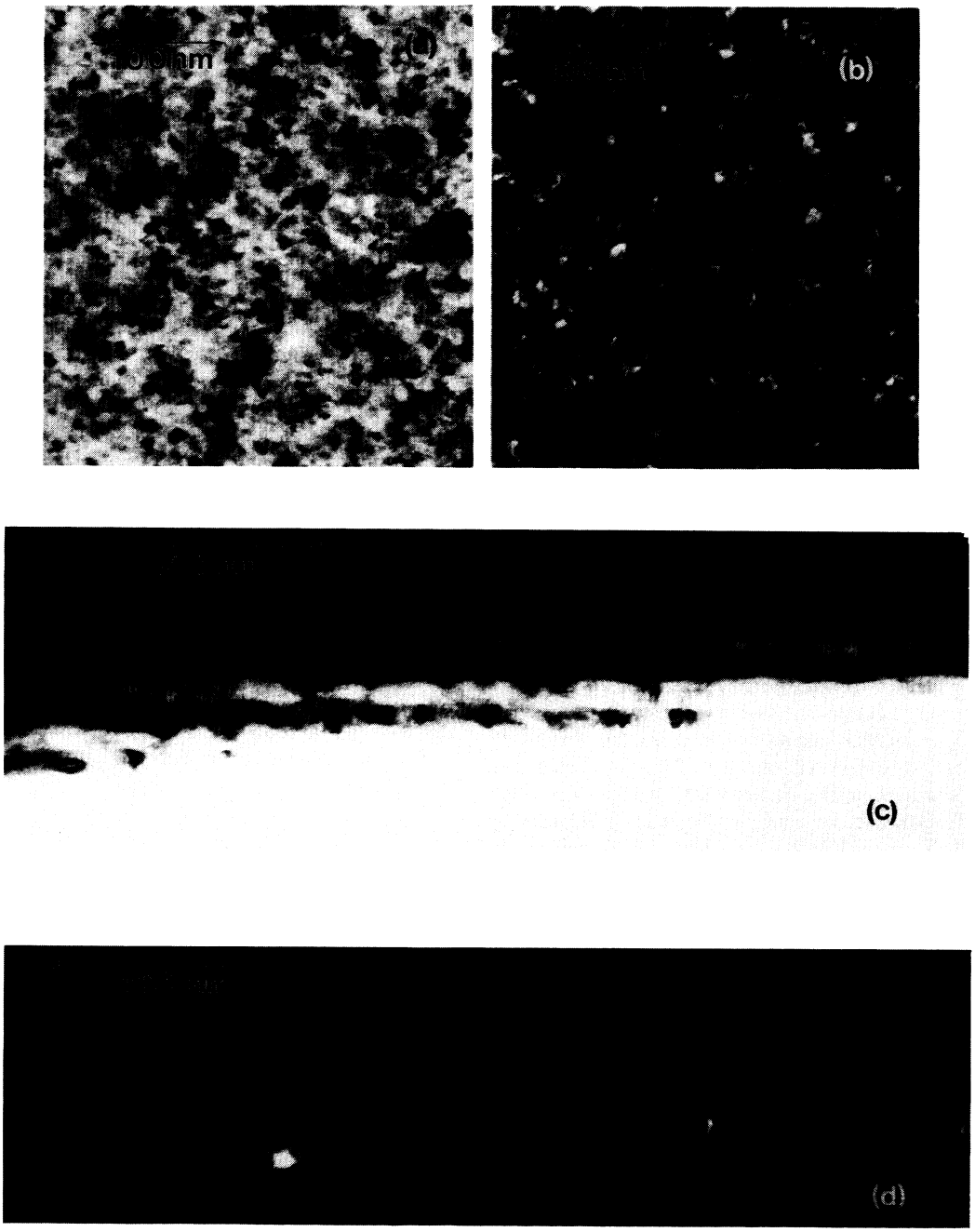

FIG. 6. TEM images of an as-prepared sample: (a) planar section, bright field; (b) planar section, dark-field Ni{111}; (c) cross section, bright field; (d) cross section, dark-field Ni{111}.

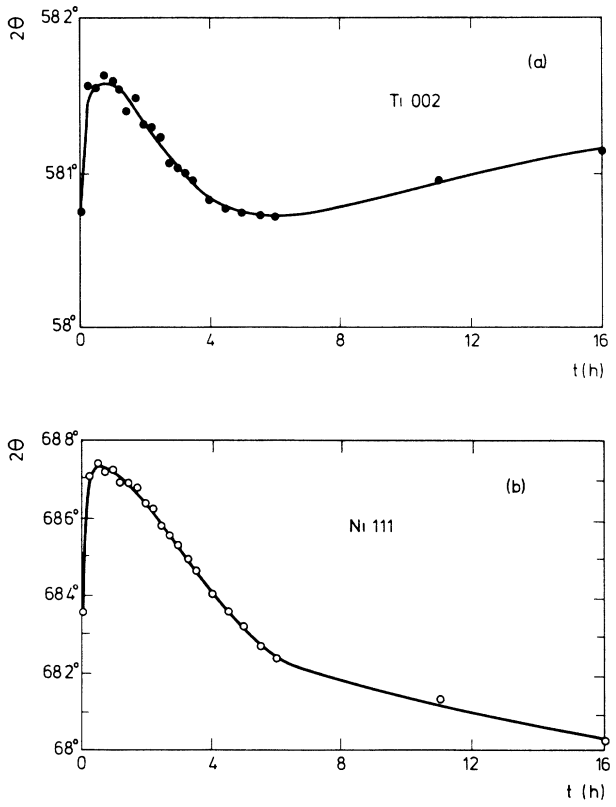

FIG. 7. Experimental peak positions as a function of annealing time, corrected for differences in diffractometer alignment: (a) Ti{002}; (b) Ni{111}.

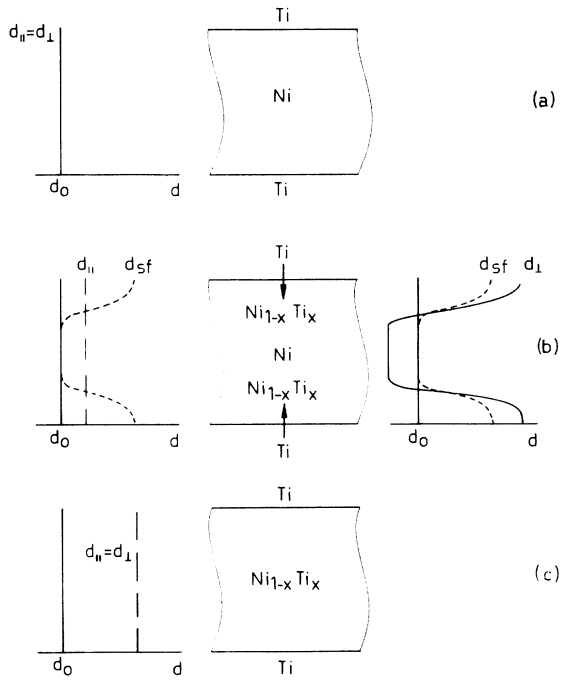

FIG. 8. Effect of Ti dissolution on the lattice spacing of the Ni crystallite. (a) A pure Ni crystal, the lattice spacing is everywhere the strain-free lattice spacing of pure Ni, d_0. (b) Initial stages of dissolution, Ti dissolved only in the top and bottom parts; the strain-free lattice spacing, d_{sf}, is a function of Ti content and thus of the position in the sublayer; the actual lattice spacing parallel to the interfaces, $d_{\parallel}$, is constant and is calculated with a balance of forces over the crystallite; the lattice spacing perpendicular to the interfaces, $d_{\perp}$, then is calculated from $d_{\parallel}$ and the strain parallel to the interfaces. (c) Ti is dissolved homogeneously; the lattice spacing is constant.

Hence, coherency strains induced by dissolution of Ti in the Ni sublayer lead to a Ni{111} peak shift in a direction opposed to that expected from straightforward application of Bragg's law on the basis of the strain-free average lattice spacing.

Eventually, compositional homogenization of the Ni sublayer [Fig. 8(c)] relaxes the coherency strains and the peak will shift to smaller scattering angles, as is observed [Fig. 7(b)]. Supposing the Ni sublayer to be homogenized after 220 h and adopting the dependence of the Ni lattice spacing on Ti content as reported in the literature,[13] about 14 at. % Ti would be dissolved in the Ni sublayer after 220 h. In view of the metastable Ni-Ti phase diagram (Fig. 1), this is possible at the applied annealing temperature of 523 K.

The increase of the maxima of the Laue satellites in the first stage of annealing is consistent with the suggested dissolution of Ti in the interface-adjacent regions of the Ni sublayers (Fig. 9, see discussion in Sec. III A).

The second-order peaks after 195 min are shown in Fig. 10. The broad and very asymmetric intensity band between 90° and 100° must be completely ascribed to the Ni{222} reflection. This is evidenced by intensity considerations and the fact that the band decreases uniformly upon tilting. The asymmetry is ascribed to the concentration variations in the Ni sublayer. A conceivable procedure for converting the peak profile for one order into that of another order in the presence of spacing variations is by application of Bragg's law to the values for the diffraction angles of the individual intensities constituting the peak profile to be transformed. This, however, implies that regions in the specimen of different composition diffract incoherently.[16] Because the spacing variations occur in coherently diffracting domains and because

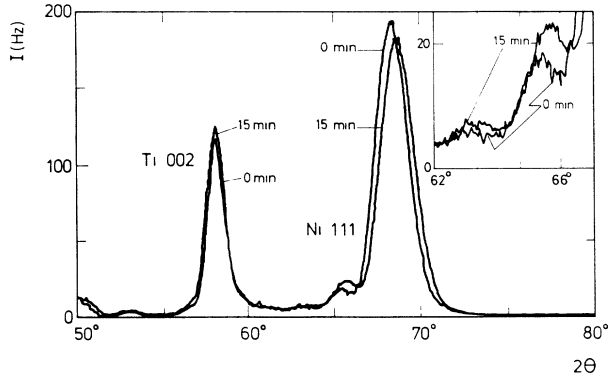

FIG. 9. Diffraction pattern of the as-prepared sample and after 15 min of annealing (Cr $K\alpha$ radiation); the inset shows the enhancement of the Laue satellites.

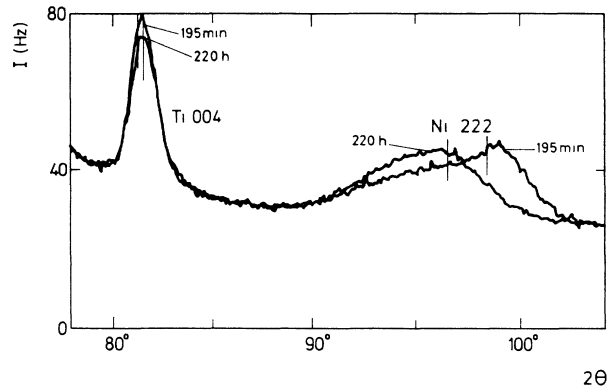

FIG. 10. Second-order peaks, Ti{004} and Ni{222}, after 195 min and 220 h of annealing (Cu $K\alpha$ radiation). The vertical lines indicate the peak positions as calculated using Bragg's law from the positions of the maxima of the corresponding Ti{002} and Ni{111} reflections.

there is additional broadening due to smallness of the domains, this procedure cannot be applied. Indeed, conversion in this manner of the Ni{222} profile into the Ni{111} profile after 195 min (Fig. 11) led to a Ni{111} profile unequal to the measured one. When the composition homogenizes upon further annealing, the Ni{222} peak should become less asymmetric, which is indeed observed (Fig. 10).

Obviously, the Ni{111} peak also becomes asymmetric upon dissolution of Ti. This is demonstrated by the parameter w_l/w_r (Fig. 12). As w_l is much more affected by Ti dissolution than w_r (also see Fig. 10), $2w_r$ instead of w_l+w_r is taken as a measure of broadening due to smallness.

C. Product-phase formation along interfaces between the sublayers and along grain boundaries in the sublayers

A disappearance of crystalline Ni and/or Ti upon annealing will be reflected by a decrease of $1/2w$ and of I_{int} (see discussion at the beginning of Sec. III). It is therefore concluded from the experimental results shown in Fig. 13 that both crystalline Ni and crystalline Ti are consumed during annealing (it will be shown in Sec. III D that the product phase is an amorphous Ni-Ti alloy).

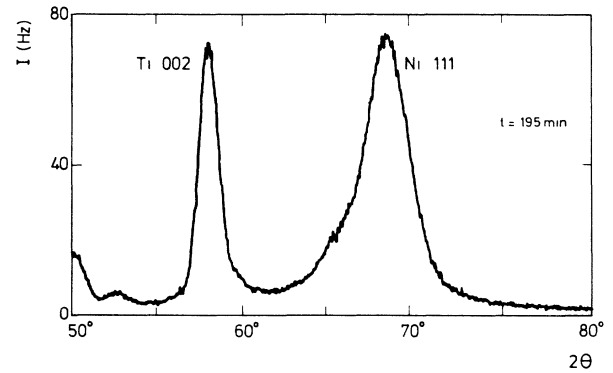

FIG. 11. First-order peaks, Ti{002} and Ni{111}, after 195 min of annealing (Cr $K\alpha$ radiation).

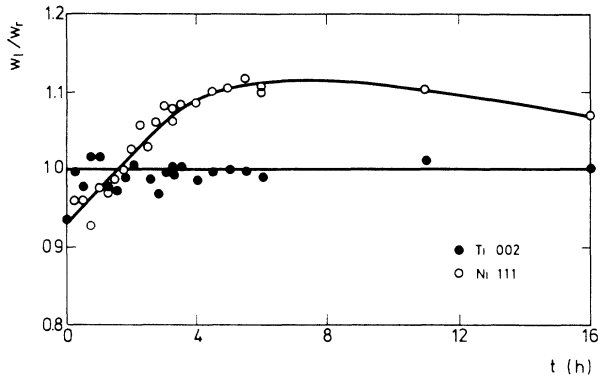

FIG. 12. Peak-asymmetry parameter w_l/w_r for Ti{002} and Ni{111} as a function of annealing time.

The minor increase of $1/2w$ for the Ti{002} peak during the first 15 min of annealing is ascribed to the annealing out of sputter-induced defects. After the removal of the structural defects, $1/2w$ can be used as a measure for

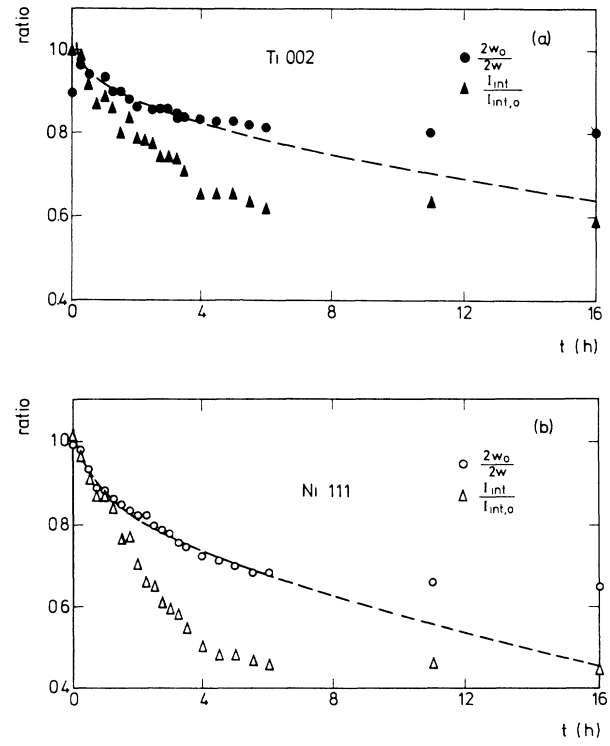

FIG. 13. Relative reciprocal linewidth $2w_0/2w$ and relative integrated intensity $I_{\text{int}}/I_{\text{int},0}$ as a function of annealing time; the dashed curve through $2w_0/2w$ is obtained by fitting Eq. (1), the "parabolic growth law," to the data points up to 4 h: (a) Ti{002}, and the fit parameters are $2w_0=1.183°$, $t_0=0.17$ h, $p=0.091$ h$^{-1/2}$; (b) Ni{111}, $2w_r$, and $2w_rI_{\max}$ have been taken for $2w$ and I_{int} (see text), and the fit parameters are $2w_{r,0}=2.286°$, $t_0=0.17$ h, $p=0.137$ h$^{-1/2}$.

the thickness of the sublayer concerned. For diffusion-controlled growth of a product phase nucleated at the Ni/Ti interfaces and growing perpendicular to them, it may be expected that the amount of phase formed is proportional to the square root of annealing time minus a possible incubation time t_0. This leads to

$$1-\frac{2w_0}{2w}=p(t-t_0)^{1/2}\ . \tag{1}$$

For up to 4 h of annealing, Eq. (1) provides a good description of the experimental data (Fig. 13).[17] With reference to the initial parabolic behavior, a retarded conversion occurs for longer annealing times; this is discussed in Sec. III F.

Upon annealing, I_{int} decreases significantly faster than $1/2w$ (Fig. 13). The integrated intensity ratio, $I_{\text{int}}(\omega=13°)/I_{\text{int}}(\omega=0°)$, for both reflections (about 0.1 for Ni{111} and 0.2 for Ti{002}) remained constant during annealing within 10%. This is within the experimental error for this ratio, and no systematic trend was observed. Furthermore, if the difference in time behavior of I_{int} and $1/2w$ would have been caused by a change in texture, this would have meant a *de*crease in sharpness of the texture, which is highly improbable as a result of annealing. Thus it is concluded that the texture of Ni and Ti did not change during annealing. It then follows that the total amounts of crystalline Ni and crystalline Ti [proportional to I_{int} (Refs. 18 and 19)] decrease faster than the respective sublayer thicknesses (proportional to $1/2w$). This difference is explained by product-phase formation also along grain boundaries in the sublayers (see Fig. 14). Grain boundaries can act as fast diffusion paths, facilitating nucleation of product phase along them. Subsequent growth of this product phase occurs in directions *parallel* to the Ni/Ti interfaces; this process will lead to a reduction of I_{int}, whereas $1/2w$ will remain constant. The quantitative argument runs as follows.

Consider a diffracting rectangular Ni or Ti crystallite with dimensions $A\times A\times Z$, with Z perpendicular to the Ni/Ti interfaces. The volume, V, is proportional to I_{int}; the sublayer thickness, Z, is proportional to $1/2w$. Hence, the average lateral size of the crystallite, A, is proportional to $(2wI_{\text{int}})^{1/2}$. Therefore the parameter $(2wI_{\text{int}}/2w_0I_{\text{int},0})^{1/2}$ is a measure for the relative (remaining) lateral size of the average parent crystallite, A/A_0. Data are shown in Fig. 15.

It follows from Fig. 15(b) that upon annealing the rate of decrease of A/A_0 is larger for specimen 1 than for specimen 2. For all other parameters discussed, there is no difference in annealing behavior between the two specimens. The difference in the behavior of A/A_0 is probably a consequence of the lateral dimensions of the crystallites in specimen 1 being smaller than those in specimen 2, leading to more product-phase formation along grain boundaries perpendicular to the Ni/Ti interfaces in specimen 1 and thus a faster decrease of A/A_0.

For quantitative interpretation of the behavior of I_{int} and $1/2w$, see Sec. IV.

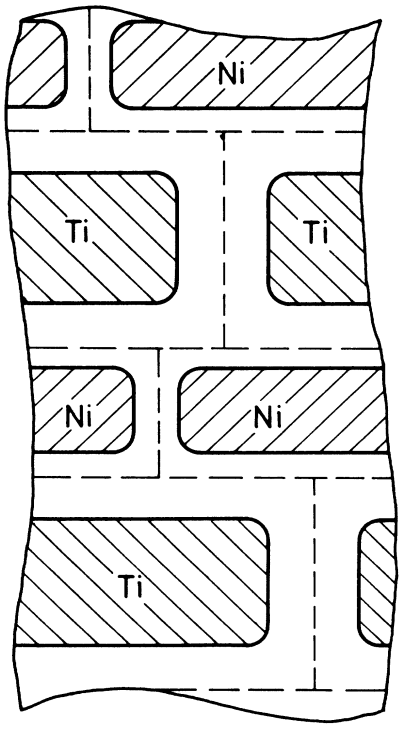

FIG. 14. Schematic drawing of a multilayer showing amorphous-phase formation along the original Ni/Ti interfaces and along the original grain boundaries in the sublayers.

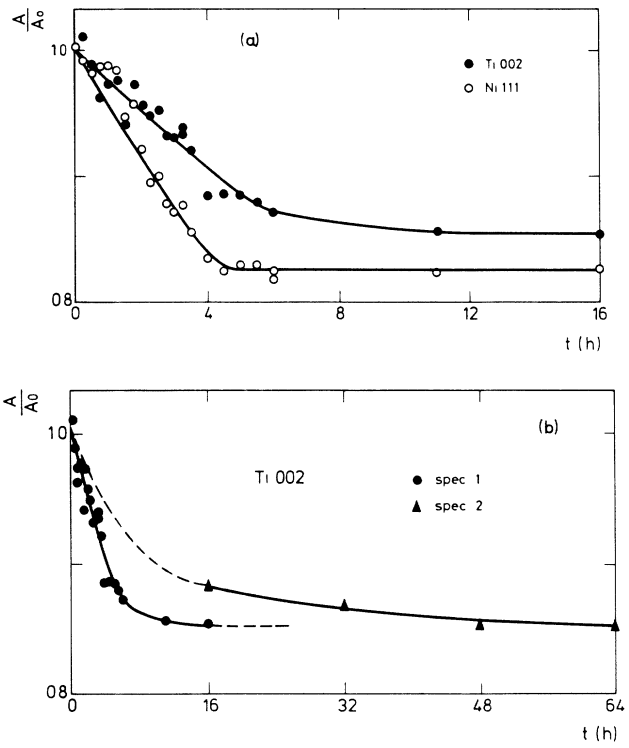

FIG. 15. Relative lateral crystallite size $A/A_0=(2wI_{\text{int}}/2w_0I_{\text{int},0})^{1/2}$ as a function of annealing time: (a) the first 16 h only, for Ti{002} and Ni{111}; (b) up to 64 h for Ti{002}, showing a difference in A/A_0 behavior between specimens 1 and 2 (similar results were obtained for Ni{111}).

D. Amorphous nature of product phase and its composition

The following observations were made.

(i) Upon annealing, the intensities of the Bragg peaks due to the parent crystalline Ni and Ti phases decrease considerably (Fig. 13).

(ii) New Bragg peaks do not appear.

(iii) An intensity band between the Ti{002} and Ni{111} peaks arises; this intensity band is best seen if the specimen is tilted [see Fig. 16(b), where $\omega=13°$], because, as compared to the diffractogram recorded at $\omega=0°$ [Fig. 16(a)], the Ti{002} and N{111} peaks are strongly reduced in intensity as a consequence of the strong texture of the crystalline Ni and Ti sublayers.

From these observations it is concluded that the product phase, whose formation follows from (i), is amorphous [(ii) and (iii)]; note that the diffracted intensity, corrected for ω-dependent geometry effects, of an amorphous product phase is not affected by tilting the specimen, as does happen for the textured crystalline parent phases [(iii)]. The maximum of the amorphous peak [$Q=(4\pi\sin\theta)/\lambda=2.988$ Å^{-1}] is in good agreement with the range reported for melt-spun amorphous Ni-Ti [$Q=2.81-3.05$ Å^{-1} (Ref. 20)]. Furthermore, the width of the amorphous peak ($\Delta Q=0.46$ Å^{-1}) is comparable with values retrieved from Ref. 21 for amorphous Ni-Ti prepared in different ways ($\Delta Q=0.47-0.51$ Å^{-1}).

Additional evidence for the amorphous nature of the product phase has been obtained recently by us from resistivity measurements. After annealing, the temperature coefficient of the resistivity has become negative between 77 and 293 K. In the Ni-Ti system, this sign is unique for amorphous Ni-Ti.[20] The TEM data also suggest amorphization [Fig. 17(b)].

It is difficult to separate intensity contributions of the

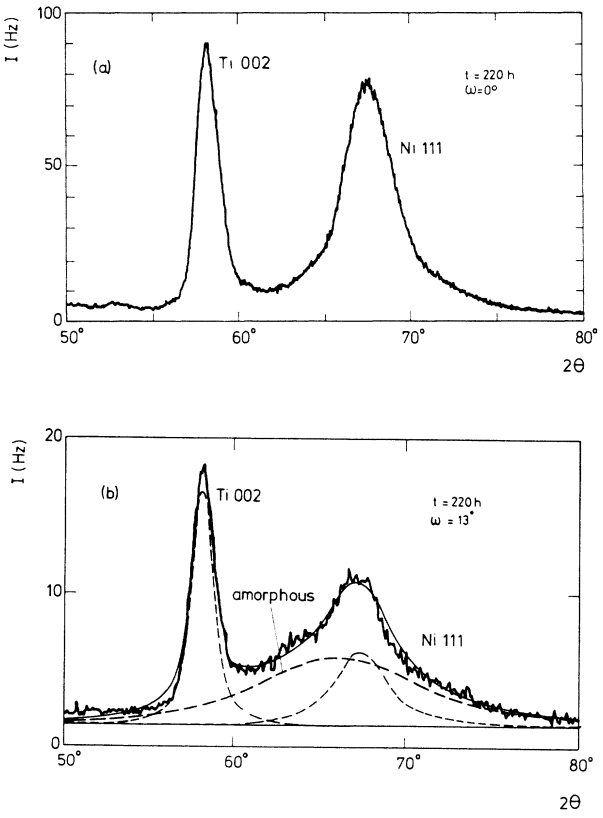

FIG. 16. Diffraction pattern after 220 h of annealing (Cr $K\alpha$ radiation): (a) $\omega=0°$; (b) $\omega=13°$, the dashed curves are three (symmetric) pseudo-Voigt functions (as implemented in the software package Siemens Diffrac−11) fitted to the data with the Ti{002} and Ni{111} integral breadths taken to be identical to those for $\omega=0°$ (this approximate decomposition of the pattern is only intended as a rough indication).

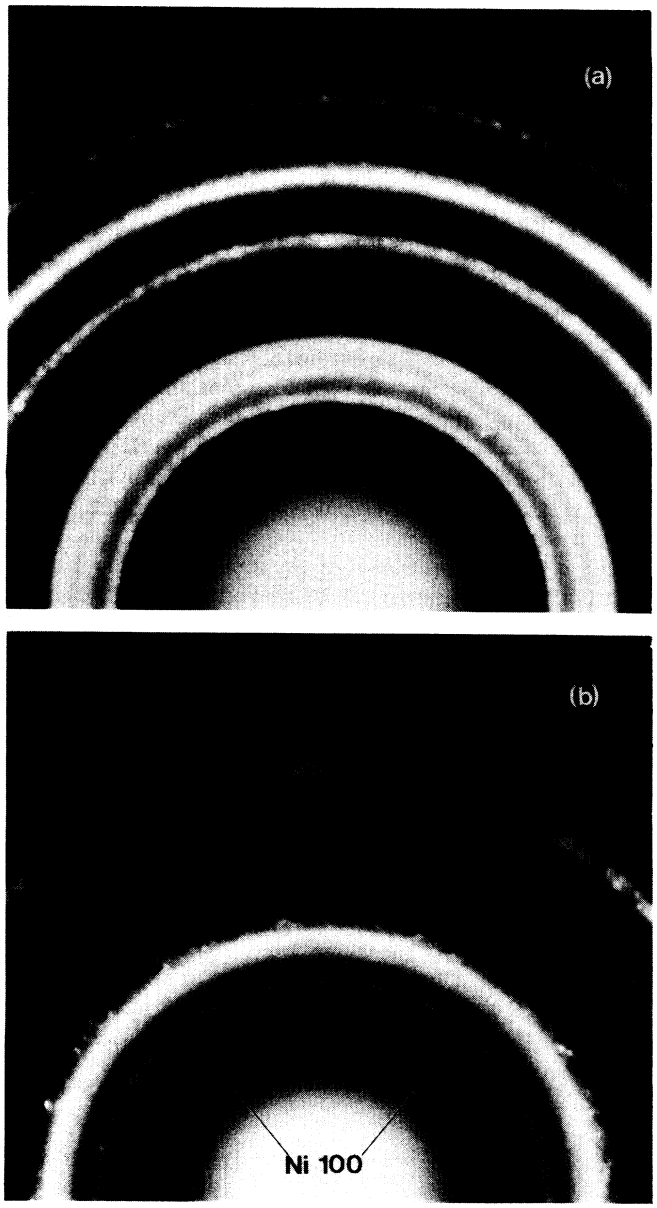

FIG. 17. Electron-diffraction patterns obtained from planar section; upon making the prints, the inner and outer parts of the patterns are exposed separately; (a) before annealing; (b) after 16 h annealing. The arrows indicate the Ni{100} diffraction ring, and a few weak spots can be discerned; note the diffuse band, which is ascribed to the amorphous phase.

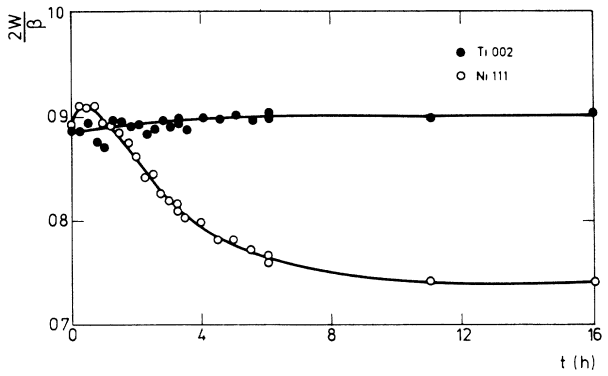

FIG. 18. Peak-shape parameter $2w/\beta$ for Ti{002} and for Ni{111} (with $2w_r$ for $2w$) as a function of annealing time.

amorphous phase and the crystalline phases in the diffractogram recorded for the untilted condition of the specimen. In general, the integrated intensity I_{int} of a peak of a crystalline phase will be overestimated. However, $2w$ and $I_{\max}$ will only be influenced slightly. Thus, the peak-shape factor $2w_r/\beta$ for Ni{111} will decrease upon annealing, as is observed (Fig. 18), erroneously suggesting a change of peak shape. As the high-angle part of the Ni{111} peak is thought not to change in shape upon annealing, $2w_r I_{\max}$ can be used as a measure for integrated intensity of the peak, rather than the (overestimate) I_{int}. The Ti{002} peak is less affected by overlap with the intensity band (Fig. 16), as is also manifested by the value of $2w/\beta$ remaining practically constant (Fig. 18, about 0.90; see Sec. III A).

The *overall* composition of the amorphous phase after a certain annealing time can be calculated from the corresponding relative decrease of I_{int} for the crystalline Ni and Ti phases and the overall composition of the specimen, provided that the amount of Ti dissolved in Ni is known. Except for the initial stage of amorphization, the amount of Ti dissolved in crystalline Ni may, in a first approximation, be neglected as compared to the amount of Ti in the amorphous product. For annealing times longer than 2 h the calculated composition is fairly constant; see results in Fig. 19. The amount of Ti in the amorphous phase is overestimated, because the Ti dissolved in crystalline Ni has been ignored. It has been calculated in Sec. III B that about 14 at. % Ti is dissolved in crystalline Ni after 220 h. Taking into account these data, a corrected value for the overall composition of the amorphous phase after 220 h is determined as $Ni_{50}Ti_{50}$, which is in the middle of the concentration range, where the amorphous phase is metastable at the annealing temperature of 523 K (Fig. 1).

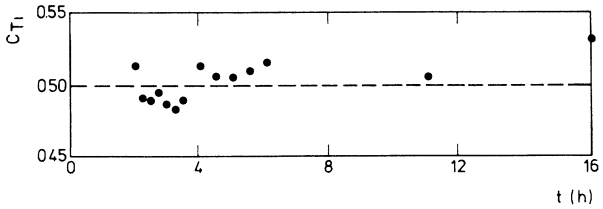

FIG. 19. Atomic fraction, c_{Ti}, of the amorphous phase as derived from the decreases in I_{int} as a function of annealing time, neglecting the dissolution of Ti in Ni. Because of the large relative errors in data calculated for short annealing times, no values are given for annealing times smaller than 2 h. The horizontal line indicates the $Ni_{50}Ti_{50}$ composition (see text).

The composition of the amorphous phase formed *at the Ni/Ti interfaces* can be deduced from the decrease of $1/2w$ for Ni and Ti. Using the data obtained upon fitting Eq. (1) to the $1/2w$ values, it follows that the atom fraction of Ti in the amorphous product phase, c_{Ti}, can be calculated according to

$$c_{Ti} = \frac{p_{Ti} c_0^{Ti}}{p_{Ni} c_0^{Ni} + p_{Ti} c_0^{Ti}} , \tag{2}$$

with $c_0^{Ni,Ti}$ as the overall Ni,Ti atomic fraction of the specimen. The result $Ni_{50}Ti_{50}$ is equal to the value for the composition calculated above from I_{int}, which is the overall composition of the amorphous phase developed along both the Ni/Ti interfaces *and* the grain boundaries in the sublayers. Hence, the amorphous phase formed along the grain boundaries in the sublayers has the same overall composition as the amorphous phase formed at the interfaces.

E. Volume contraction and stress development

The relative molar volume change, $\Delta V_m/V_m$, on transforming x Ni and y Ti into Ni_xTi_y can be expressed as

$$\frac{\Delta V_m}{V_m} \equiv \frac{V_m^{Ni_xTi_y} - (xV_m^{Ni} + yV_m^{Ti})}{xV_m^{Ni} + yV_m^{Ti}} , \tag{3}$$

where V_m^i denotes the molar volume of phase i.

Data for $\Delta V_m/V_m$ as calculated from published data for V_m^i for the stable crystalline phases[13] and for amorphous $Ni_{40}Ti_{60}$ (Ref. 22) are presented in Fig. 20. Realiz-

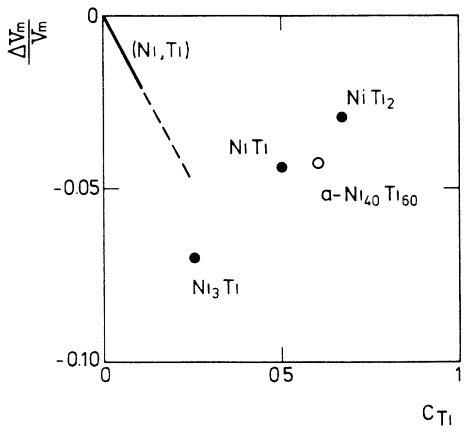

FIG. 20. Relative molar-volume change for the formation of a product phase out of parent crystalline Ni and Ti, $\Delta V_m/V_m$, for the stable crystalline intermetallic compounds and for amorphous $Ni_{40}Ti_{60}$ (c_{Ti} denotes the atomic fraction of Ti).

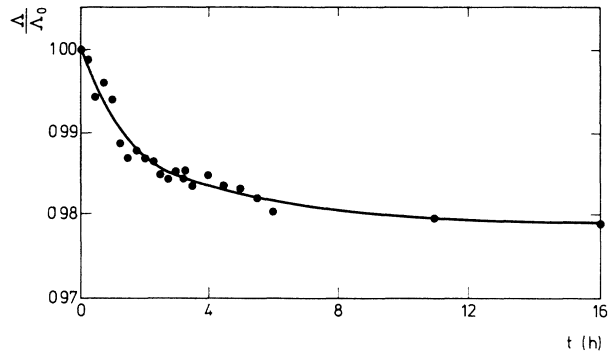

FIG. 21. Relative composition-modulation length, Λ/Λ_0, as a function of annealing time.

ing that the product phase has a composition $Ni_{50}Ti_{50}$, it is expected that amorphous-phase formation leads to a decrease of volume of the multilayer.

If stress effects can be ignored and since the lateral dimensions of the multilayer remain constant (as imposed by the substrate), the expected volume contraction of the multilayer on amorphization is realized entirely by a decrease of thickness of the multilayer. The experimentally observed multilayer period, Λ, indeed decreases during the transformation (Fig. 21). Experimental values for $\Delta V_m/V_m$ can be calculated as a function of annealing time, t, from Eq. (3) using

$$xV_m^{\mathrm{Ni}}+yV_{\mathrm{m}}^{\mathrm{Ti}}=C[\Lambda_0-\Lambda^{\mathrm{cr}}(t)]\ , \tag{4a}$$

and

$$V_m^{\mathrm{Ni}_x\mathrm{Ti}_y}=C[\Lambda(t)-\Lambda^{\mathrm{cr}}(t)]$$

$$\text{with } \Lambda^{\mathrm{cr}}(t)=\frac{I_{\mathrm{int}}^{\mathrm{Ni}}(t)}{I_{\mathrm{int},0}^{\mathrm{Ni}}}Z_0^{\mathrm{Ni}}+\frac{I_{\mathrm{int}}^{\mathrm{Ti}}(t)}{I_{\mathrm{int},0}^{\mathrm{Ti}}}Z_0^{\mathrm{Ti}}\ , \tag{4b}$$

where C is a constant, and Z_0^{Ni} and Z_0^{Ti} are the original sublayer thicknesses. The results are shown in Fig. 22. Taking the composition of the amorphous phase as $Ni_{50}Ti_{50}$ (see Sec. III D), it follows from a comparison of Figs. 20 and 22 that the theoretical and experimental molar-volume contractions agree fairly well.

Until now, stress development in association with

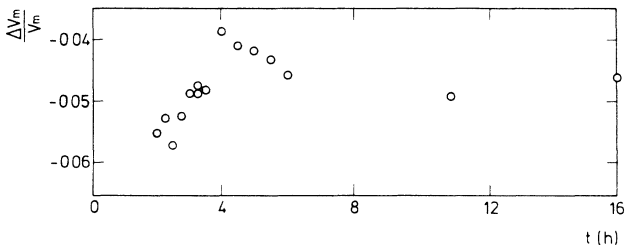

FIG. 22. Relative molar-volume change for the formation of the (amorphous) product phase out of crystalline Ni and Ti, $\Delta V_m/V_m$, as a function of annealing time as derived from the decrease of Λ/Λ_0 [Eqs. (3) and (4)]. Because of the large relative errors in data calculated for short annealing times, no values are given for annealing times smaller than 2 h.

change of volume has not been considered, i.e., the misfit due to volume change is fully accommodated plastically. However, cohesion of multilayer and substrate (discussed in subsection 1 below) and of neighboring phases in the multilayer (discussed in subsection 2 below) can bring about (partial) elastic accommodation of the volume misfit, implying stress development. In the following a step-by-step discussion is given of such stress development in the multilayer.

1. *Overall effect of transformation*

First, the effect of the overall volume contraction due to amorphization will be considered. Because the substrate is orders of magnitude thicker than the multilayer, a tendency to overall volume contraction of the multilayer will lead to an overall tensile stress in the multilayer parallel to the multilayer-substrate interface, if (part of) the volume misfit is accommodated elastically. By measuring the change of the curvature of the specimen during annealing, applying Fizeau interferometry, the relative change of the overall stress in the multilayer can be tracted. Upon annealing, the sample becomes more and more concave as viewed from above. Hence, a tensile stress indeed develops in the multilayer on amorphization.

Stress in the multilayer can also be generated by heating or cooling the specimen. Upon heating the specimen from room temperature to the annealing temperature, the corresponding thermal misfit between multilayer and substrate results in a compressive stress in the multilayer. Obviously, this effect is, in principle, reversible. However, if stress relaxation occurs at the annealing temperature, a subsequent cooling to room temperature will result in a net thermal stress in the multilayer at room temperature (at which Fizeau interferometry has been performed). By this reasoning, the tensile stress observed at room temperature after 4 h of annealing might be ascribed to the thermal misfit due to cooling, implying completed stress relaxation at the annealing temperature. However, as will be shown in subsection 2, this stress relaxation is a relatively slow process as compared to the measured rapid development of tensile stress in the multilayer. It is concluded that the progress of amorphization is associated with the development of a significant tensile stress in the multilayer, as a result of (partial) elastic accommodation of the volume misfit due to amorphization.

In view of the large radius of curvature of the specimen, a state of plane stress with equal principal stresses can be assumed. Then, straightforward application of elasticity theory shows that, *as compared to the stress-free condition*, the relative volume of the multilayer is changed by the presence of a stress $\sigma_{\parallel}$ parallel to the multilayer-substrate interface by an amount $(\Delta V/V)_{\mathrm{el}}$ according to

$$\left[\frac{\Delta V}{V}\right]_{\mathrm{el}}=\left[\frac{1-2\nu}{E}\right]2\sigma_{\parallel}\ , \tag{5}$$

where ν and E are Poissons's ratio and Young's modulus, respectively. Because $\sigma_{\parallel}>0$ (tensile stress) and $\nu<\frac{1}{2}$, it

follows that $(\Delta V/V)_{el} > 0$. Hence, the volume contraction strived for by the amorphization is obviously not fully realized if the associated volume misfit is (partly) accommodated elastically. The lateral dimensions of the substrate are unchanged by the presence of the state of stress because the balancing compressive stress in the substrate has a negligible value due to the relatively large thickness of the substrate. Then the experimental magnitude of $\Delta V_m/V_m$, as derived from the measured change of Λ (Fig. 22), will be somewhat smaller than that predicted theoretically (Fig. 20).

From the *overall* (macro)stress acting on the multilayer, no conclusions can be drawn about the stress distribution in the multilayer; the latter will be discussed next.

2. *Local effect of transformation*

The molar volume of the amorphous phase is larger than that of the crystalline Ni phase (also with Ti dissolved) and smaller than that of the crystalline Ti phase. In the same way as discussed above for the overall misfit between multilayer and substrate, (partial) elastic accommodation of this local molar-volume misfit may be expected for amorphization along the interfaces which originally separate Ni and Ti, but which upon amorphization separate amorphous product phase and crystalline parent phases. It can thus be imagined that, parallel to the interfaces, a tensile stress would develop in the remaining Ni and a compressive stress in the remaining Ti. It should be kept in mind that, in view of the discussion in subsection 1, the overall stress parallel to the interfaces in the multilayer (as obtained by summing the forces parallel to the interfaces acting on a section perpendicular to them) is not zero, but of tensile nature. In the present work this summation of forces cannot be performed using experimental data, among other things, because the stress in the amorphous phase is not known.

The behavior of the lattice spacings of the Ni and Ti phases (Fig. 7) includes effects due to stress development. As discussed in Sec. III B, the change of the Ni{111} spacing is governed by Ti dissolution, which impedes the stress analysis for the Ni layer.

The initial Ti{002} spacing indicates the presence of a compressive stress parallel to the Ni/Ti interfaces, which is ascribed to the sputtering process (Sec. III A). From Fig. 7(a) it follows that during the first 15 min of annealing some relaxation of this compressive stress takes place. Upon further annealing, when amorphization sets in significantly, a compressive stress in the crystalline Ti sublayer develops, in accordance with the prediction. Upon continued annealing, when the amorphization rate decreases, relaxation processes become dominant and the compressive stress decreases [i.e., the Ti{002} spacing perpendicular to the interfaces becomes smaller; Fig. 7(a)].

Another extreme for stress development in the multilayer is obtained upon considering only amorphization along the grain boundaries in the sublayers. The inward flux of Ni atoms along Ti grain boundaries may be larger than the outward flux of Ti atoms. If the volume increase due to the excess flux overcompensates the volume decrease due to amorphization, a compressive stress develops in the Ti sublayer.

F. Decrease of transformation rate

The linear relationship between $1/2w$ and $(t-t_0)^{1/2}$ [cf. Eq. (1)] holds during the first 4 h of annealing. At longer annealing times the reaction slows down until it virtually stops after 16 h, although there still is crystalline Ni and Ti (Fig. 13). It is proposed below that the termination of amorphization is a consequence of ordering in the fcc (Ni,Ti) solid solution.

In the electron-diffraction pattern of a (planar view) TEM specimen after 16 h, a weak diffraction ring occurs at the location of the forbidden Ni{100} reflection [Fig. 17(b)]. This reflection can be due to ordering in the fcc (Ni,Ti) solid solution. It is suggested that the amorphous phase is thermodynamically unstable with respect to the ordered alloy.

A similar phenomenon has been noted in Ni/Zr diffusion couples, in which, upon prolonged annealing, no further amorphization occurs, but a crystalline intermetallic compound nucleates.[23]

IV. AMORPHIZATION BY BULK AND GRAIN-BOUNDARY DIFFUSION

The relatively simple model[2] for growth of the amorphous phase as singular layers thickening perpendicular to the Ni/Ti interfaces without alloying taking place in the parent crystalline phases does not hold (Sec. III). Two complications have been found: (1) Ti does dissolve metastably in the Ni phase, and (2) amorphization also occurs along grain boundaries in the sublayers. In a separate paper[24] a model is presented for quantitative analysis of amorphization simultaneously along the original interfaces and along the grain boundaries within the sublayers. The model takes into account the difference between the kinetics of bulk diffusion and of grain-boundary diffusion.

The experimental data allow one to distinguish between the effects of both diffusion paths: (i) Growth of the amorphous phase as layers parallel to the original Ni/Ti interfaces, by bulk diffusion perpendicular to these interfaces, is measured by the decrease of $1/2w$, and (ii) growth of the amorphous phase along the grain boundaries in the sublayers, due to grain-boundary diffusion, is measured by the decrease of $(2wI_{int})^{1/2}$. The diffusion coefficient in the amorphous phase developing along the Ni/Ti interfaces, D_{am}, is thus calculated as about 1.0×10^{-22} $m^2 s^{-1}$, from the (parabolic) rate constants [Eq. (1)] pertaining to the first 4 h of annealing. The chemical diffusion coefficient, D_{am}, is smaller than the tracer-diffusion coefficient of Ni in α-Ti (Ref. 4) and larger than the chemical diffusion coefficient in fcc (Ni,Ti) solid solutions.[25]

The observed *continued* growth of amorphous phase along the grain boundaries involves fast-diffusion paths remaining active upon prolonged annealing. This may be explained as follows. The boundaries between the crystallites in the sublayers are likely to be of high-angle type,

as indicated by TEM analysis (see Figs. 6 and 17). High-angle grain boundaries generally have a relatively open structure. For example, it is suggested from a comparison of grain-boundary energy and vacancy-formation energy that such high-angle grain boundaries could be crudely modeled as a lattice plane with a vacancy concentration of approximately 25%.[26] The relatively high porosity pertaining to the open structure of the originally present high-angle boundary may be maintained for at least the first hours of annealing, during which significant amorphization occurs.

Applying the model mentioned,[24] it follows from the roughly linear decrease of A/A_0 with annealing time (Fig. 15) that the grain-boundary diffusion coefficient, D_{GB}, is approximately 100 times larger than D_{am}. The "grain-boundary" (or fast path) diffusion processes in the Ni and Ti sublayers cannot be considered to be independent, because, if the net fluxes by grain-boundary diffusion into the sublayers are different (as a consequence of different grain-boundary diffusion coefficients and different grain-boundary densities), the resulting volume misfit will lead to stress development and plastic deformation. Amorphization along the grain boundaries will then be rate-controlled by the sublayer with the "slowest" grain boundary and/or the smallest grain-boundary density, and by the rate of plastic accommodation. The grain-boundary densities of the Ti sublayer and of the Ni sublayer are about equal (cf. Sec. III A). Hence, if the observed development of a compressive stress in the Ti sublayer upon annealing (cf. Sec. III E) is caused by amorphization along the "grain boundaries," it follows that the Ti "grain boundaries" are the "fastest." Apparently, diffusion of Ni in Ti "grain boundaries" is faster than diffusion of Ti in Ni "grain boundaries."

V. CONCLUSIONS

Annealing at 523 K of polycrystalline Ni/Ti multilayers leads to amorphization both at the Ni/Ti interfaces and at the grain boundaries in the Ni and Ti sublayers. Concurrently, Ti dissolves in crystalline Ni.

A. Ti dissolution

The initially inhomogeneous dissolution of Ti in the Ni sublayer induces an elastic strain profile in the Ni sublayer. This leads to a predicted and observed initial shift of the Ni{111} peak position in a direction opposed to that expected for strain-free dissolution of Ni in Ti. Other diffraction phenomena associated with this Ti dissolution are enhancement of the Laue satellites at the low-angle side of the Ni{111} reflection, as well as asymmetrical line broadening. Upon continuous annealing the Ni layer homogenizes and the coherency strains relax.

The dissolution of Ti in Ni indicates that the mobility of the larger atom (Ti) cannot be neglected with respect to that of the smaller atom (Ni).

B. Amorphization

Product-phase formation along both the Ni/Ti interfaces and the grain boundaries is exhibited by the decrease of the integrated intensities of the crystalline Ni and Ti reflections and their increasing broadening. Diffraction analysis showed the product phase to be amorphous.

The occurrence of distinct "grain-boundary amorphization," also along the Ni grain boundaries, also indicates that the mobility of the slowest atom (Ti) cannot be neglected as compared to that of the fastest atom (Ni).

The continued growth of the amorphous phase along the original grain boundaries implies that fast-diffusion paths remain active. This is ascribed to conservation of the open structure originating from the initially present (high-angle) grain boundaries.

Amorphization leads to an overall tensile stress in the multilayer parallel to the multilayer-substrate interface, as indicated by Fizeau interferometry. The stress distribution in the multilayer is such that a compressive stress occurs in the Ti sublayers. Upon prolonged annealing, when the amorphization rate decreases, stress relaxation becomes dominant over stress buildup.

C. Kinetics of amorphization

The interdiffusion coefficient in the amorphous phase (1.0×10^{-22} $m^2 s^{-1}$ at 523 K) is about 100 times smaller than that pertaining to the fast-diffusion paths in the sublayers.

The amorphization practically stops before all crystalline Ni or all crystalline Ti has been converted. This is attributed to ordering in the (Ni,Ti) solid solution.

ACKNOWLEDGMENTS

We are indebted to Dr. Ir. Th. H. de Keijser and Ir. O.B. Loopstra for stimulating discussions. The Centre of Submicron Technology of the Delft University of Technology made available the sputtering facilities. X-ray facilities were provided by Ing. N. M. v. d. Pers and Dr. Ir. Th. H. de Keijser. Ing. E.J.A. van Dam carried out electron-probe microanalyses. Dr. G. Pennock showed us how to prepare cross-sectional TEM specimens and C. D. de Haan provided TEM facilities. The resistivity measurements were performed by A. van der Graaf. Financial support from the Stichting voor Fundamenteel Onderzoek der Materie [Foundation for Fundamental Research of Matter (The Netherlands)] is gratefully acknowledged.

[1]R. B. Schwarz and W. L. Johnson, Phys. Rev. Lett. **51**, 415 (1983).
[2]W. L. Johnson, Prog. Mater. Sci. **30**, 81 (1986).
[3]K. Zöltzer and R. Bormann, J. Less-Common Met. **140**, 335 (1988).
[4]G. M. Hood and R. J. Schulz, Philos. Mag. **26**, 329 (1972).
[5]B. M. Clemens, Phys. Rev. B **33**, 7615 (1986).
[6]J. F. Jongste, M. A. Hollanders, B. J. Thijsse, and E. J. Mit-

temeijer, Mater. Sci. Eng. **97**, 101 (1988).
[7]M. A. Hollanders and B. J. Thijsse, J. Less-Common Met. **140**, 33 (1988).
[8]M. A. Hollanders, C. G. Duterloo, B. J. Thijsse, and E. J. Mittemeijer (unpublished).
[9]B. E. Warren, *X-Ray Diffraction* (Addison-Wesley, Reading, MA, 1969).
[10]P. F. Miceli, D. A. Neumann, and H. Zabel, Appl. Phys. Lett. **48**, 24 (1986).
[11]*Powder Diffraction Data* (Joint Committee on Powder Diffraction Standards, Swarthmore, PA, 1960).
[12]J. A. Thornton and D. W. Hoffman, J. Vac. Sci. Technol. **14**, 164 (1977).
[13]W. B. Pearson, *Handbook of Lattice Spacings and Structures of Metals and Alloys* (Pergamon, Oxford, 1958), p. 791.
[14]R. B. Bracewell, *The Fourier Transform and Its Applications,* 2nd ed. (McGraw-Hill/Kogakusha, Tokyo, 1978), p. 433.
[15]*Landolt-Börnstein, Numerical Data and Functional Relationships in Science and Technology, New Series, Band III/11, Elastic, Piezoelectric, Pyroelectric, Electrooptic Constants, and Nonlinear Dielectric Susceptibilities of Crystals,* edited by K. H. Hellwege (Springer, Berlin, 1979).
[16]E. J. Mittemeijer and R. Delhez, in *Accuracy in Powder Diffraction,* Natl. Bur. Stand. (U.S.) Spec. Publ. No. 567, edited by S. Block and C. R. Hubbard (U.S. GPO, Washington, D.C., 1980), p. 271.
[17]Using Scherrer's equation (cf. beginning of Sec. III), with $\beta=2w_0/0.886$ (the numerical constant holds if the line profile conforms to a Laue function), and the $2w_0$ values obtained by fitting, the initial Ni and Ti sublayer thicknesses are found to be 6.2 and 11.2 nm, respectively. These values differ from those derived from the overall composition (EPMA) and the composition-modulation wavelength (XRD): 7.2 and 17.2 nm, respectively (see Sec. III A). The presence of coherently diffracting domains smaller than the sublayer thickness can explain this discrepancy, particularly for the Ti sublayer (this is consistent with the observation that Laue satellites are not present for the Ti{002} peak, cf. Fig. 9 and Sec. III A). However, the *relative* change of $1/2w$, an average over all diffracting domains, may still be used as a measure for the transformed fraction of the sublayer thickness.
[18]Here, the decrease in the mean atomic-scattering factor upon dissolution of Ti in Ni for the Ni{111} reflection is neglected. The largest error due to this effect is expected at the end of the annealing treatment, when the largest amount of dissolved Ti occurs. Adopting literature values for the atomic scattering factors (Ref. 19), it is calculated that I_{int} of the Ni{111} reflection is decreased by 8.6% when 14 at.% Ti is dissolved (Ti content after 220 h; see Sec. III B). This is much smaller than the observed difference between I_{int} and $1/2w$ after 220 h.
[19]*International Tables for X-ray Crystallography, Vol. IV. Physical and Chemical Tables* (Kynoch, Birmingham, England, 1962), p. 201.
[20]K. H. J. Buschow, J. Phys. F **13**, 563 (1983).
[21]M. S. Boldrick, D. Lee, and C. N. J. Wagner, J. Non-Cryst. Solids **106**, 60 (1988).
[22]S. H. Whang, L. T. Kabacoff, D. E. Polk, and B. C. Giessen, J. Mater. Sci. **15**, 247 (1980).
[23]W. J. Meng, C. W. Nieh, E. Ma, B. Fultz, and W. L. Johnson, Mater. Sci. Eng. **97**, 87 (1988).
[24]M. A. Hollanders, B. J. Thijsse, and E. J. Mittemeijer (unpublished).
[25]A. Ya. Shinyaev, Phys. Metal. Metallogr. **21**, 76 (1966).
[26]J. L. Meijering, Acta Metall. **14**, 251 (1966).

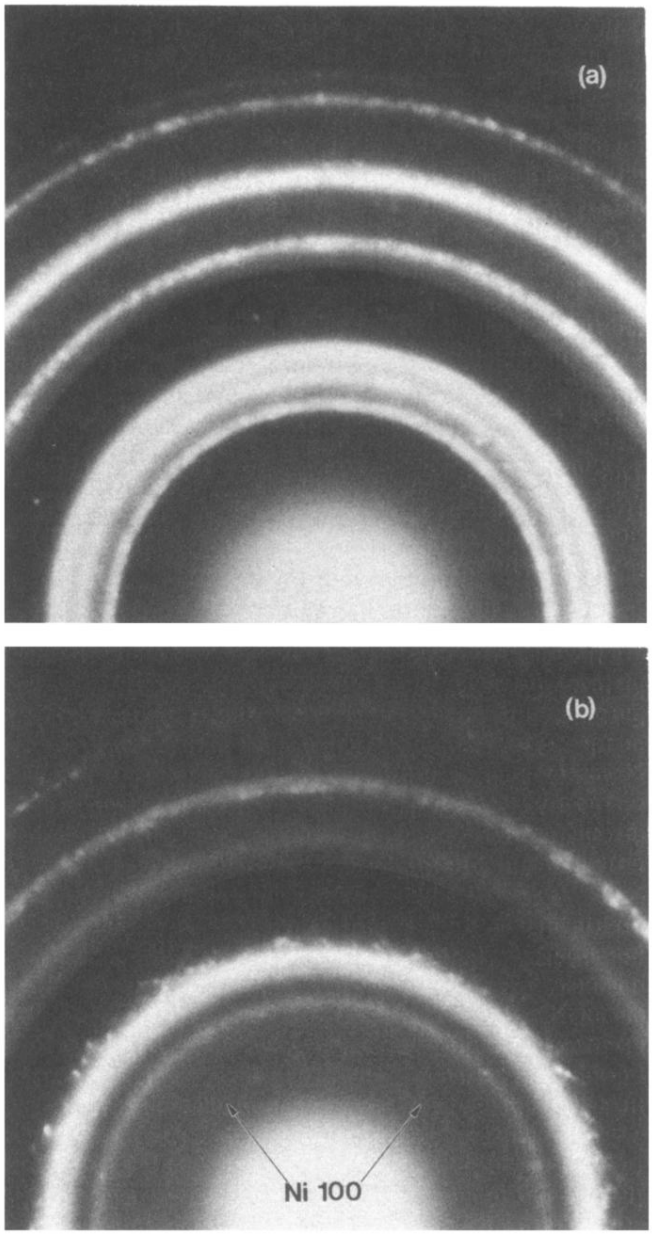

FIG. 17. Electron-diffraction patterns obtained from planar section; upon making the prints, the inner and outer parts of the patterns are exposed separately; (a) before annealing; (b) after 16 h annealing. The arrows indicate the Ni{100} diffraction ring, and a few weak spots can be discerned; note the diffuse band, which is ascribed to the amorphous phase.

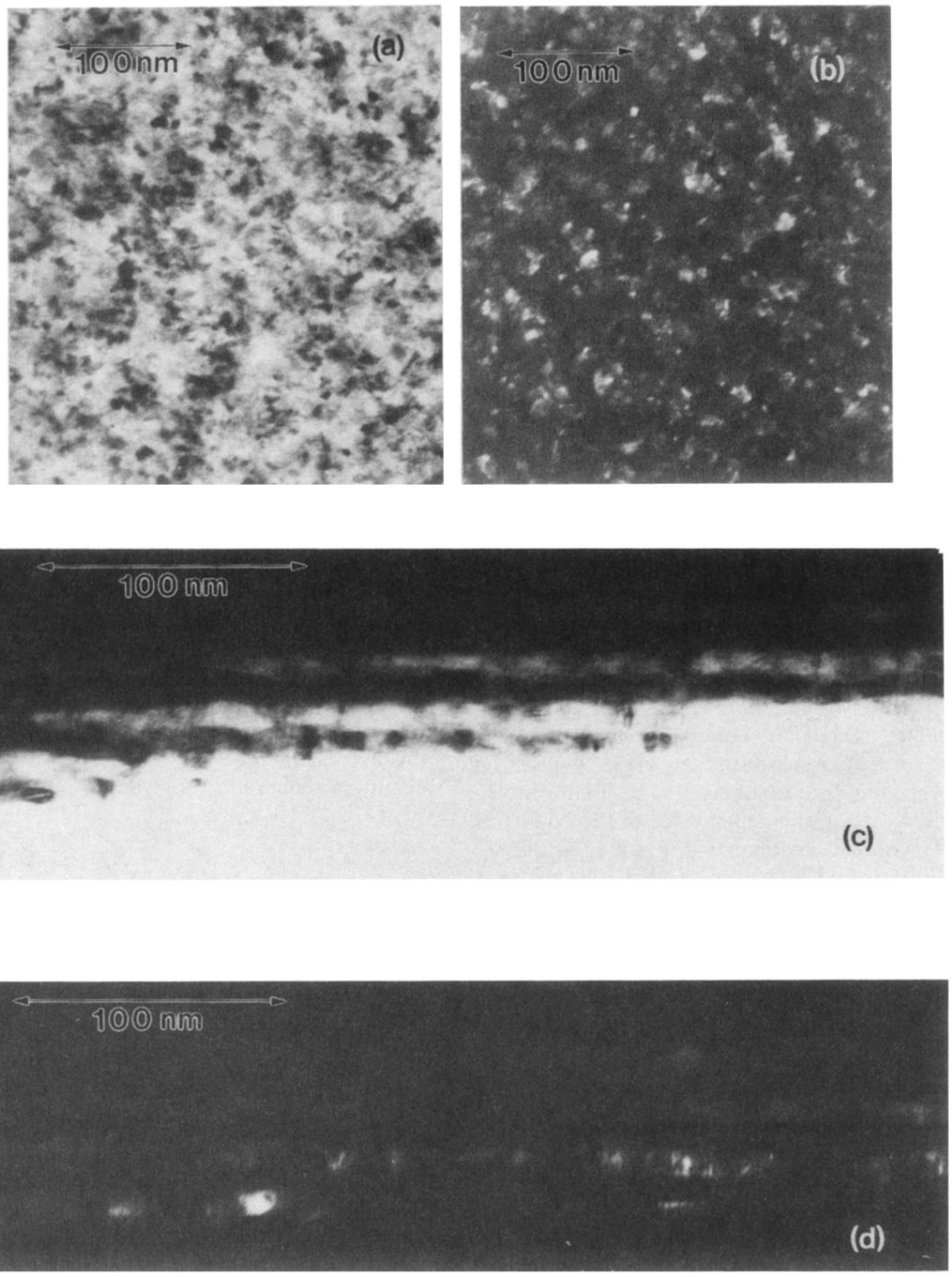

FIG. 6. TEM images of an as-prepared sample: (a) planar section, bright field; (b) planar section, dark-field Ni{111}; (c) cross section, bright field; (d) cross section, dark-field Ni{111}.